

Application of Microprobe Analysis to the Reconstruction and Characterization of Dendritic Structures

JOSEF DOMITNER, ABDELLAH KHARICHA, MENGHUAI WU,
and ANDREAS LUDWIG

The electron probe microanalyzer (EPMA or “microprobe”) is a powerful tool for nondestructive chemical analysis of solid materials. The work presented in this article proves the concept of reconstructing three-dimensional (3-D) dendritic structures in steel based on 5 two-dimensional (2-D) EPMA concentration maps. The EPMA measurements are focused on the concentration distribution of Mn, which has a distinct microsegregation tendency in steel. Because the concentration maps must be taken from different depths of the investigated sample, serial sectioning of the sample is required for each microprobe measurement. These measured concentration maps are processed with a commercial software tool to smooth and to merge the maps, as well as to consider the temperature gradient that occurred during solidification on the microsegregation pattern. Afterward, the concentration maps are stored in a 3-D array, and the neighboring array entries with the same predefined threshold concentration value are connected with surfaces to build a 3-D dendritic structure. Because the concentration of certain alloying elements in the solid phase increases during the solidification process, it is possible to visualize the dendritic growth by increasing the solid fraction. Finally, a simple correlation was used to relate the specific surface area to the solid volume fraction of the dendrites. The obtained 3-D structures can be used for subsequent investigations in finite-element (FE) or computational fluid dynamics (CFD) simulation tools.

DOI: 10.1007/s11661-012-1120-x

© The Minerals, Metals & Materials Society and ASM International 2012

I. INTRODUCTION

IN the field of numerical simulation, such as computational fluid dynamics (CFD) or structural mechanics, the three-dimensional (3-D) geometric representation of the investigated structure is a crucial input parameter. Particularly, this is the case if complex-shaped solidification microstructures are investigated using numerical simulation, because microstructural features (*e.g.*, number and connectivity of particles or dendrites) might affect the simulation results distinctly. Such features can only be determined exactly from 3-D microstructure representations.^[1] For example, fluid-flow simulations through reconstructed dendritic networks indicated that the direction-dependent permeability is influenced strongly by the interfacial surface area, which varies with the fraction of solid.^[2]

If a certain structure has a well-defined geometry, then it is relatively straightforward to create its representation by using computer-aided design tools. In most engineering cases, this may apply. However, the evolving microstructures undergoing some growth phenom-

ena can exhibit structures with complex shapes. Therefore, they cannot be described easily with simple geometric relations. To make such structures available for numerical simulations, they are captured using different analysis techniques. Commonly, computed X-ray microtomography^[3–6] or serial sectioning of the sample combined with micrograph stacking is used. The generated geometric information is then imported into the simulation software.

An overview about first serial sectioning approaches carried out in the last century to study the shape of metal phases such as ferrite, cementite, or perlite is given by Kral *et al.*^[7] The described approaches had the fundamental disadvantage that the manual sectioning and image acquisition procedures were extremely tedious. Nevertheless, in 1983 DeHoff already predicted that serial sectioning would become an important method to generate and to evaluate 3-D metallic microstructures by overcoming this awkward problem.^[1]

Li *et al.*^[8] used the serial sectioning technique to obtain detailed 3-D microstructure images of an Al-alloy reinforced with Si-particles. Therefore, optical micrographs taken from a series of two-dimensional (2-D) sections were digitalized and then stacked together computationally. Prior to removing each section from the sample, fiducial pyramidal hardness indents of known proportions were made to enable the alignment of the sections and to measure the removed material thickness at each pass. Chawla *et al.*^[9,10] went one step further. They used the microstructure obtained with a similar serial sectioning technique for subsequent

JOSEF DOMITNER, PhD Student, is with the Christian Doppler Laboratory for Multiphase Modeling of Metallurgical Processes, University of Leoben, A-8700 Leoben, Austria. Contact e-mail: josef.domitner@unileoben.ac.at ABDELLAH KHARICHA, Senior Scientist, MENGHUAI WU, Associate Professor, and ANDREAS LUDWIG, Professor, are with the Chair of Simulation and Modeling of Metallurgical Processes, University of Leoben.

Manuscript submitted March 30, 2011.

Article published online March 22, 2012

finite-element (FE) studies of the deformation behavior of particle-reinforced metal matrix composites.

Nowadays, fully automated serial sectioning systems combined with computer-aided image reconstruction are available to visualize 3-D dendritic structures. These systems allow the removal of thin material layers in the order of a few micrometers.^[11–13] An automated micromiller system was used by Voorhees and colleagues for capturing dendritic microstructures in AlCu and PbSn alloys with the aim of characterizing their morphology and of investigating coarsening phenomena.^[14–16] Madison *et al.* used RoboMET.3D (UES, Inc., Dayton, OH), which is a fully automated metallographic polishing system, to characterize the solidification front of Ni-based single crystals. Structural features such as primary and secondary dendrite arm spacings or the solid fraction depending on the mushy zone height were determined.^[17] These 3-D single-crystal structures were then used for fluid flow modeling and related permeability investigations.^[2]

The described mechanical serial sectioning techniques are suitable to obtain microstructure representations with an edge length of several hundred micrometers. To reconstruct 3-D ceramic microstructures of only few micrometers, Schaffer *et al.* used an electron probe microanalyzer (EPMA) equipped with a focused ion beam (FIB) for automated sample material removal.^[18] The elemental analysis of each section created was performed with energy-dispersive X-ray spectrometry. The obtained 2-D elemental composition maps were used together with back-scattered electron images of the section surfaces to create 3-D reconstructions.

However, the conventional serial sectioning method delivers only the geometric representation of the dendrites after solidification, but the varying dendritic shape during progressive solidification is not captured. This is deficient for a detailed investigation of solidification processes, because most parameters to describe a dendritic structure (*e.g.*, solid–liquid interface, volume fraction of solid, and permeability) change strongly with the evolution of the dendrites. To capture their changing shape during solidification, comparatively elaborate *in situ* observations (*e.g.*, high-speed or synchrotron X-ray microtomography^[19,20]) are required, which are applicable only to investigate the samples of laboratory scale.

Besides experimental reconstruction methods, numerical models were applied to generate dendritic structures for subsequent simulation work. Spittle and Brown^[21] computed 2-D cross sections of growing columnar dendrites using a cellular automation (CA) model. The obtained structures were used to calculate the evolution and the coarsening behavior of dendrites. Jarvis *et al.*^[22] developed a combined cellular automaton-finite difference technique to simulate the evolution of 3-D dendritic shapes during solidification. Based on the obtained structures, the influences of the solid fraction and of the geometry on the permeability were studied.^[23] Rappaz and Gandin proposed a method based on the CA technique to predict 2-D dendritic grain growth in castings considering uniform and nonuniform temperature fields.^[24,25] To calculate nonuniform temperatures,

the CA technique was combined with the FE method. The 2-D model was extended to the third dimension to predict 3-D dendritic grain growth in metals.^[26]

Another possibility to simulate dendritic growth in two dimensions as well as in three dimensions provides the phase-field method.^[27–29] Combining the phase-field method with fluid-flow simulations (*e.g.*, based on the Lattice-Boltzmann method) can be applied to evaluate the permeability of microstructures.^[30]

The numerical microstructure generation allows following the evolution of the dendritic profile during solidification. However, depending on the used simulation method, different thermophysical input data (*e.g.*, cooling conditions, alloying element compositions, *etc.*) are required. These input data are often not available or they are complex to describe industrial casting processes and alloys properly. Therefore, assumptions and simplifications have to be made that might influence the simulation results.

Hence, it would be more convenient to acquire an appropriate estimation of the dendritic growth by investigating a completely solidified sample at room temperature. Under such conditions, the quantity to be measured must correlate with the evolving dendritic shape during the solidification process, and it must be observable postmortem, *i.e.*, after the solidification event has occurred. For example, the concentration of a certain alloying element inside the solidified metal represents such a “growth-dependent” quantity. Therefore, the basic idea of the current reconstruction method is to measure the concentration distribution inside of a solid sample with a microprobe. The concentrations measured in different layers are then related to the solid fractions that have occurred during solidification.

In steel, the solubility for most alloying elements of practical use is higher inside the melt than inside the forming solid. These elements are rejected from the solid phase during the solidification process, whereas their content increases continuously in the liquid phase. Thus, the first forming solid has lower alloying element contents than the solid forming out of the highly enriched melt at the end of solidification.^[31] This segregation tendency at the microscale level is used for the reconstruction method presented in this article. After gathering several concentration patterns for the alloying element manganese (Mn) from a completely solidified sample, the influences of the temperature gradient and of the curvature on the concentrations are calculated. Then, identical concentration values are connected with surfaces. These isoconcentration surfaces represent the dendritic structure at a certain stage of solidification, assuming that coarsening effects are negligible. Hence, it is possible to visualize the dendrites and to provide the geometry data as a function of elemental composition.

Notice that the method presented in this study to reconstruct dendritic structures is based on the investigation of a totally solidified sample. Therefore, the “solid phase” is represented by the solid sample domain containing lower concentrations than the threshold concentration predefined to visualize the dendrites. However, the interdendritic “liquid phase” is

represented by the solid sample domain containing higher concentrations than the threshold concentration.

II. RECONSTRUCTION PROCEDURE

A schematic overview of the reconstruction procedure presented in this article is given in Figure 1. The procedure covers the sample preparation, the microprobe measurements, and the concentration map processing. Notice that steps (b) through (d) were performed five times.

A. Sample Preparation

During the continuous casting process of steel, the surface of the cast strand is cooled rapidly with water. A steep temperature gradient along the strand's thickness occurs that causes a fine microstructure formation and oriented columnar dendritic growth from the surface toward the center. Hence, cropping a sample parallel to this growth direction beneath the strand surface ensures that the sample contains entire dendrites and not fragmented parts. For this reason, the investigated sample, which had a cross sectional area of approximately 3×3 mm, was taken 35 mm below the surface of a 285-mm-thick slab cut off from the continuous casting strand. The sample was aligned parallel to the dendritic growth direction. Figure 2 shows schematically the sample position inside the solidified continuous casting slab.

To prepare this sample for the following microprobe measurements, it was embedded into a low-melting eutectic alloy, composed of tin and bismuth.^[32] This embedding material ensures the required conductivity of electricity between the sample holder inside the microprobe and the sample itself. The material is resistant against the electron beam of the microprobe, which

allows for effective measurement in the embedding area surrounding the investigated sample. The considerable difference in the measured Mn concentrations between the sample and the embedding material can be used to detect the sample's boundaries and to align each concentration map along these boundaries afterward.

Attention must be paid to the exact orientation of the sample face chosen to be sectioned. For rectangular-shaped samples, this face must be situated perpendicular to its four neighboring faces and perpendicular to the sectioning direction as well. If this is not the case, then the edge alignment method used to position the measured concentration maps for the 3-D reconstruction may result in artificially slanted structures. To obtain the required perpendicularity, the sample used for the current investigations was prepared with a semiautomated milling machine with micrometer adjustment prior to embedding.

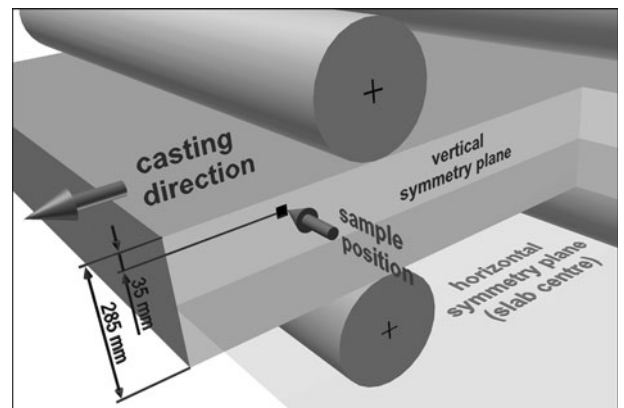


Fig. 2—Position of the investigated sample inside the continuous casting slab.

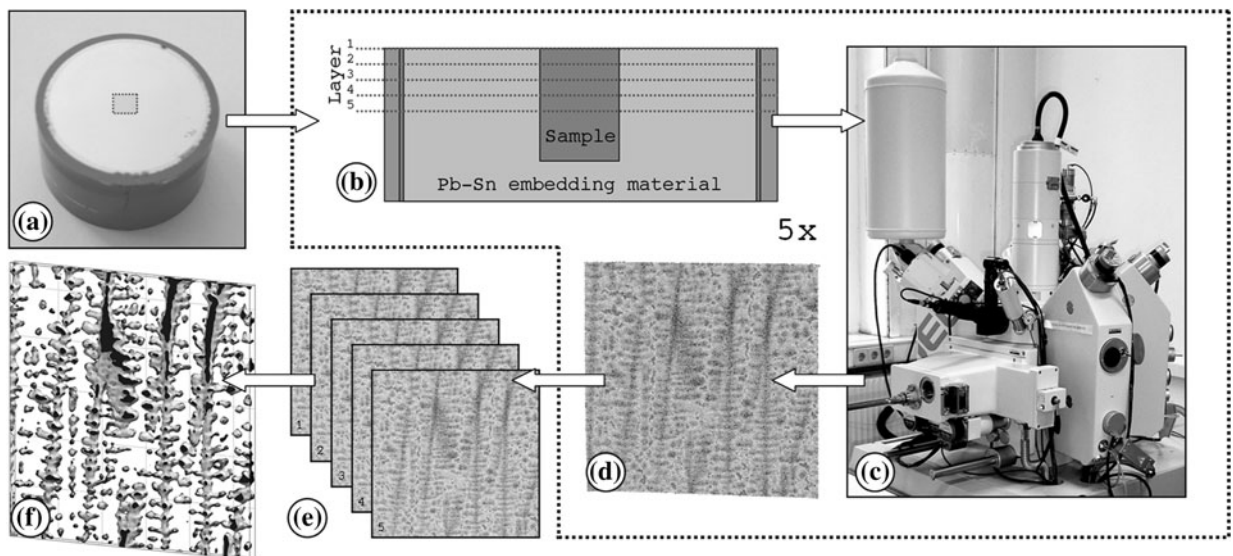


Fig. 1—Schematic overview of the presented reconstruction procedure; (a) sample taking and embedding, (b) preparing the sample for the measurement (removing a defined layer thickness and surface polishing), (c) microprobe measurement with WDS, (d) concentration map processing, (e) map alignment, and (f) reconstruction of the dendritic structure.

Clean and well-polished sample surfaces are an essential prerequisite to obtain accurate microprobe analysis results. To achieve this and to remove a layer of defined thickness from the sample, the surface to be analyzed was polished with a monocrystalline, 3- μm diamond suspension on a satin-woven, natural silk cloth first. This first polishing step afforded fast material removal. Then, the final polishing to finish the sample's surface was accomplished with a monocrystalline, 1- μm diamond suspension on a porous neoprene cloth. According to this procedure, a material layer of 25 μm ($\pm 3 \mu\text{m}$) thickness was removed using a semiautomated polishing machine. The layer thickness was checked manually with a digital indicating caliper at the center as well as at the four corners of the polished area. The described polishing procedure was performed to prepare the sample for each of the microprobe measurements. However, grinding the sample's surface was only necessary for the initial preparation after embedding to remove the deep scratches caused by sample cutting.

The distance between the microprobe maps and, therefore, the layer thickness to be removed from the sample depend on the feature size of the microstructure to be investigated and on the availability of the microprobe. For example, decreasing the distance by a factor of $\frac{1}{2}$ would double the number of microprobe maps. Thus, the time required to measure these maps for a structure of certain thickness would be doubled as well. In the used steel sample, primary (λ_1) and secondary (λ_2) dendrite arm spacings were in the order of $\lambda_1 \approx 500 \mu\text{m}$ and $\lambda_2 \approx 100 \mu\text{m}$, respectively. Tertiary dendrite arms were not observed. Because the sectioning direction was chosen to be parallel to the primary dendrite trunks, approximately 20 slices between adjacent dendrites might theoretically be achieved with a layer distance of 25 μm . This turned out to be sufficient for resolving also secondary dendrite arms between the primary dendrites in the investigated sample. However, decreasing the distance between the measured maps in the order of $\frac{1}{2}$ might be useful for subsequent detailed investigations.

Table I. Conditions and Basic Settings for the Microprobe Measurements

Analyzed element	Manganese (Mn)
Analyzing crystal material	Lithium fluoride
Acceleration voltage	15 kV
Electron beam current	250 nA
Preset value for the probe diameter:	0 μm (focused)
Dwell time per measurement point:	120 ms
Interval between measured points in horizontal x and y direction:	5 μm
Number of measured points	660 \times 660
Investigated total area per map	3300 \times 3300 μm^2
Required measurement time per map:	\sim 16 h

Table II. Nominal Chemical Composition (wt pct) of the Investigated Steel

C	Si	Mn	P	S	Cr	Ni	Cu	Mo	Ti	V	Nb	W	N	Al
0.182	0.360	1.170	0.008	0.001	0.170	0.270	0.170	0.002	0.002	0.001	0.022	0.015	0.008	0.036

B. Microprobe Measurements

The reconstruction method presented in this article is based on a set of five concentration maps, measured with wavelength dispersive spectrometers (WDSs) in a JEOL 8200 microprobe (JEOL Ltd., Tokyo, Japan). Each of these maps, taken from different depths of the investigated steel sample, consists of 660 \times 660 pixels. Each of these pixels represents a measured concentration of Mn on a small square area of 5 \times 5 μm . The main conditions and basic settings for the performed measurements are listed in Table I.

Table II gives an overview about the nominal chemical composition of the steel used for the investigations. Obviously, the concentration of Mn is higher than the concentrations of the other alloying elements. Microprobe concentration maps indicated that Mn has the most distinct segregation behavior in the sample compared with the other elements listed in Table II. Because this is essential for the presented method, concentration maps of Mn were used for the dendritic reconstruction. However, focusing on other alloying elements might be suitable for steels with different compositions.

Figure 3 shows one of the original concentration maps of Mn, obtained with the JEOL 8200 microprobe. The different grayscale levels represent the detected Mn concentrations. The black frame surrounding this grayscale map is from the extremely low Mn content of the embedding material. This difference in concentration allows the detection of the map boundaries and, therefore, an exact alignment of each map along these boundaries.

C. Concentration Map Processing

The maps obtained at the microprobe comprise thousands of pixels with their corresponding concentra-

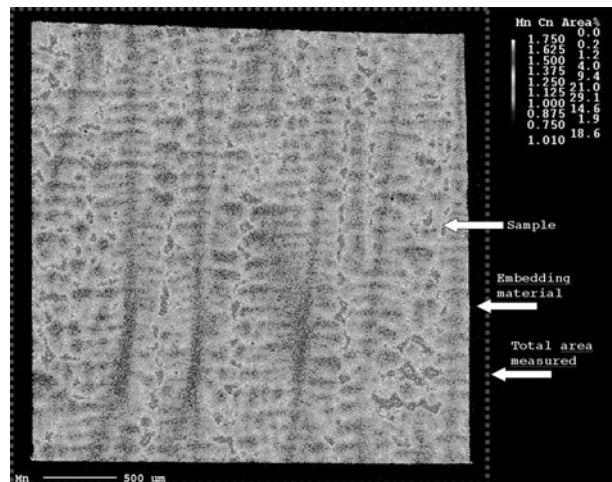


Fig. 3—Typical measured concentration map for Mn.

tion values. It is typical for the microprobe mapping method used in this study that discontinuous concentration transitions between adjacent pixels occur. Thus, connecting the concentrations directly after the measurement would create uneven instead of smooth surfaces. Hence, a preliminary smoothing of each concentration map was necessary, which was performed in two steps using the MATLAB software package (MathWorks, Natick, MA).

First, undesired peak values of concentration were removed from the measured maps. For example, minute holes, nonmetallic inclusions, or impurities on the sample's surface may cause concentration peaks, if the electron beam passes them during the measurement. Because such peaks are not connected immediately with the occurring segregations during the growth of the dendritic structure, it is necessary to remove them from the measured maps. For this purpose, a median filter, expressed by Eq. [1], was used.^[33] In a second step, a Gaussian filter was applied to the median filtered maps to achieve smooth concentration transitions required for the reconstruction. The Gaussian filter is defined by Eq. [2].^[34]

$$C_{S'}(x, y) = \text{median} \{C_S(x + i, y + j)\}_{(i,j) \in R_{x,y}} \quad [1]$$

Table III. Map Filter Parameters

Size of the median filter area	9 × 9 pixels (45 × 45 μm)
Size of the Gaussian filter area	9 × 9 pixels (45 × 45 μm)
Standard deviation σ of the Gaussian filter:	2 pixels (10 μm)

$$C_{S''}(x, y) = \sum_{(i,j) \in R_{x,y}} C_{S'}(x + i, y + j) \cdot e^{-\frac{i^2 + j^2}{2\sigma^2}} \quad [2]$$

C_S represents the concentration at a certain pixel measured with the microprobe, $C_{S'}$ stands for the concentration after applying the median filter, and $C_{S''}$ is the concentration after applying the Gaussian filter. The local filter coordinates i and j are valid only inside the filter area $R_{x,y}$, which surrounds a certain pixel at the global Cartesian map coordinates x and y . The chosen parameters for both of these filter types are summarized in Table III.

After performing the filter operations, the smoothed concentration maps were stored inside a 3-D array, one single map per array layer. The outer frame of each map (frame width 55 μm) was cut off to ensure that only the concentration values from the sample itself and not from the surrounding embedding material were stored. The final concentration array and, therefore, the structure created from the array data had a total size of 550 × 550 × 5 pixels or 2750 × 2750 × 100 μm, respectively.

D. Considering the Temperature Gradient

At the surface of the solidifying dendrite, a certain solidus temperature T_S corresponds to a specific solidus concentration $C_{S''}$, as shown schematically in Figure 4. Focusing on the Mn in steel, the solidus concentration increases “onionskin like” with advancing solidification and, therefore, with decreasing temperature. Hence, connecting immediately all measured concentrations to obtain the dendritic surface would imply that the

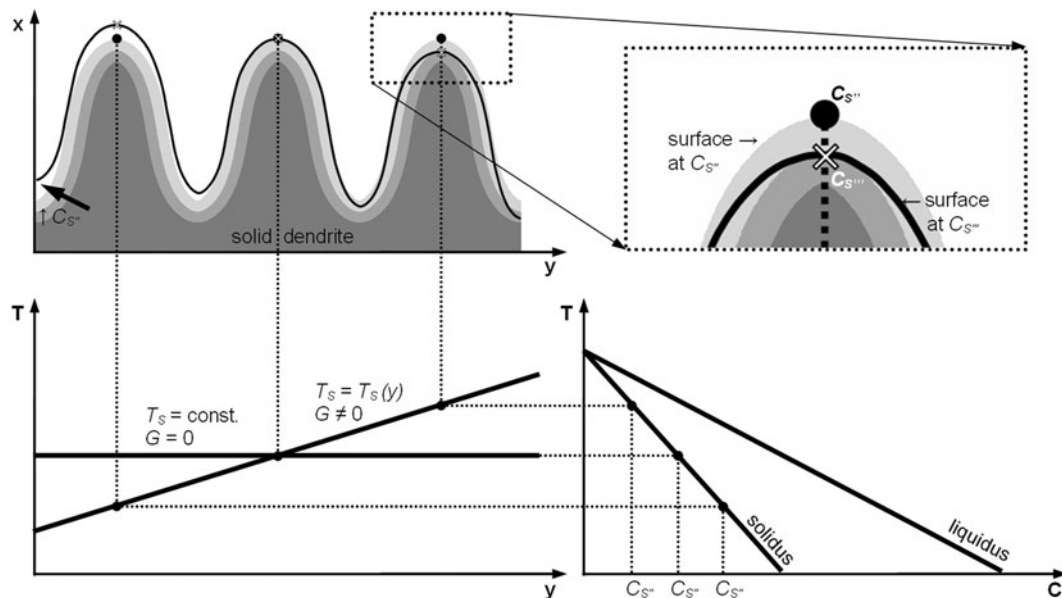


Fig. 4—Influence of a nonuniform temperature field on the surface concentration. With advancing solidification, the Mn concentration inside the solid dendrite increases, as shown schematically by the onionskin-like gray shadings. Considering a constant temperature field ($G = 0$) and neglecting the curvature effect, a certain solidus concentration $C_{S'}$ indicates the position of the dendritic surface at a certain moment of solidification. If the temperature field is nonuniform because a gradient occurs ($G \neq 0$), then $C_{S''}$ at the surface varies. Hence, the solidus concentration $C_{S''}$, which takes the temperature gradient into account has to be calculated instead. The black contour shows the dendritic surface at $C_{S''}$, which differs from the gray shaded surface at $C_{S'}$.

investigated steel sample was exposed to a spatial uniform temperature field during the solidification process. However, in steel continuous casting, the temperature increases rapidly from the water-cooled strand surface toward the hot center, which results in a steep temperature gradient along the strand thickness. Therefore, the taken sample, although it has a small size of 3×3 mm, does not experience a uniform temperature field at a certain moment of time. Hence, the temperature gradient G must also be considered in the reconstruction procedure of the dendritic structures. Depending on the local solidus temperature, the concentrations C_S^m are calculated, which differ from the measured and processed concentrations C_S^r . Based on C_S^m , it is finally possible to reconstruct the surface of the dendritic structures.

Because it is impossible to obtain the temperature field inside of the strand by analyzing the solidified metal after the casting process, the required data have to be determined by *in situ* measurements or appropriate numerical simulation studies. In this work, the strand temperature was estimated with the commercial CFD simulation software FLUENT (ANSYS, Inc., Canonsburg, PA) to avoid cost-intensive measurements. For that purpose, the upper half of a horizontal 25-m-long and 0.285-m-thick continuous casting strand was modeled in two dimensions with the preprocessing tool GAMBIT (ANSYS, Inc.). The boundary conditions and material properties applied to perform the simulation reflect the industrial casting conditions. The Eulerian two-phase solidification model^[35] used for the FLUENT calculations is a simplified form of the three-phase model described by Ludwig and Wu.^[36,37] Whereas this

general model comprises liquid melt, columnar dendrites, and equiaxed crystals, the equiaxed phase is neglected in the current simulations.

Figure 5 shows the temperature field inside the simulated continuous-casting strand. It is obvious that the temperature increases from the strand surface to the center. The dashed line has a vertical distance of 35 mm from the surface, which corresponds to the vertical position of the taken sample. The temperature T along this line and the corresponding temperature gradient G are also depicted in Figure 5. At $X \approx 1.8$ m and $X \approx 3.3$ m, the dashed horizontal line intersects with two curved isolines indicating the solid fractions $f_S = 0.1$ and $f_S = 0.9$ inside the strand (because of numerical limitations, $f_S = 0.0$ and $f_S = 1.0$ are not calculated in the model used in this study). The domain enclosed by both isolines is called the “mushy zone”, which consists of liquid and solid steel. Because dendritic solidification of a sample taken 35 mm below the surface is of interest, the current analysis focuses on this mushy zone in the range between $X \approx 1.8$ m and $X \approx 3.3$ m, which is marked with the hatched area in Figure 5. Inside this area, the temperature gradient G decreases rapidly with increasing f_S , as depicted in Figure 6.

It is impossible to comprise the temperature gradient influence on the measured concentration patterns directly with the information of Figure 6, because f_S and therefore the corresponding value of G are unknown prior to reconstructing the dendritic structure. In the current work, a remedy against this predicament was achieved by using computational thermodynamics. The relation between f_S and the concentration of Mn in the solid C_S^{Mn} was computed using the commercial

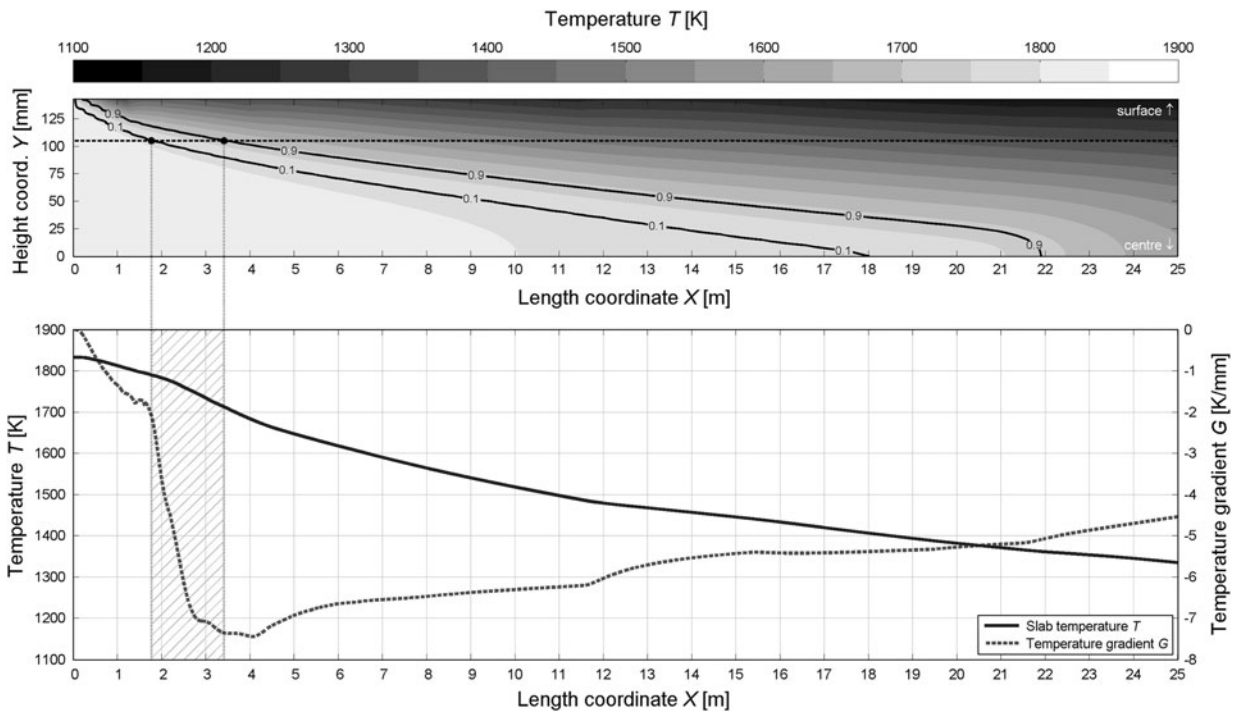


Fig. 5—Temperature field inside of the simulated continuous casting strand (for appropriate imaging, the length coordinate is scaled with a factor of 1:25), temperature and temperature gradient profiles at a depth of 35 mm below the strand surface; simulation performed with FLUENT.

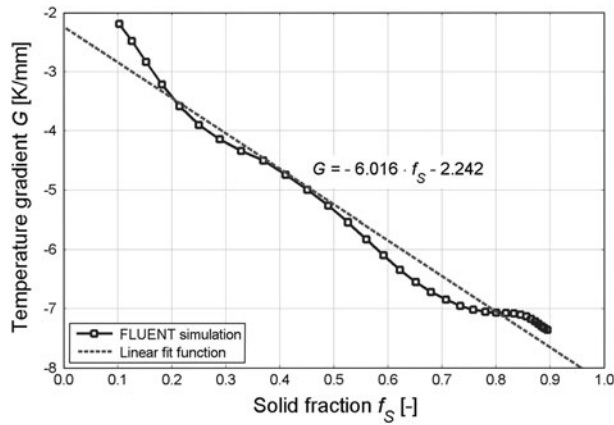


Fig. 6—Temperature gradient vs solid fraction inside of the mushy zone at a depth of 35 mm below the strand surface.

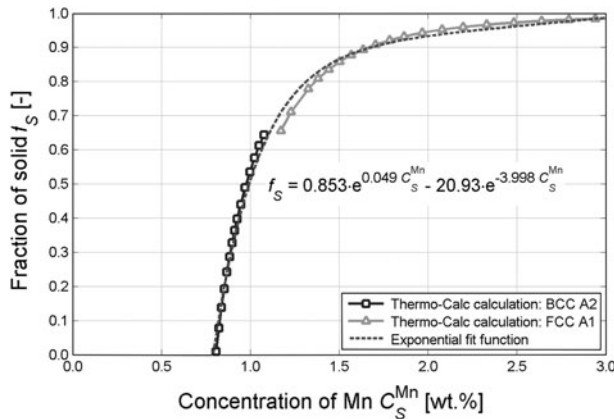


Fig. 7—Solid fraction vs concentration of Mn; calculation performed with Thermo-Calc Classic.

software package Thermo-Calc Classic, database SSOL4 (Thermo-Calc, McMurray, PA).^[38] This relation is shown in Figure 7. Hence, it was possible to estimate G for each map pixel based on the measured and smoothed concentrations C_S^Mn . The performed calculation procedure can be summarized as follows: $C_S^Mn \rightarrow f_s(C_S^Mn) \rightarrow G(f_s) \rightarrow C_S^Mn(G)$. Additionally, Thermo-Calc enabled the estimation of m^{Mn} characterizing the relation between C_S^Mn and temperature T . It is suitable to approximate m^{Mn} with constant values of $m_{bcc}^{Mn} = -90$ K/wt pct for the body-centered cubic (bcc) phase and $m_{fcc}^{Mn} = -34$ K/wt pct for the face-centered cubic (fcc) phase, as shown in Figure 8. The performed calculation was based on the entire chemical composition of the investigated steel, because all alloying elements influence the solidification behavior.

Based on the estimation of $G(C_S^Mn)$ and m^{Mn} , the concentrations C_S^Mn were then corrected with a concentration difference ΔC_G (Eq. [3]). The application of Eq. [3] is justified because the concentration map coordinate y is parallel to the temperature gradient G and, therefore, parallel to the dendritic growth direction.

$$C_S^Mn(y) = C_S^Mn - \Delta C_G = C_S^Mn - \frac{y}{m^{Mn}} \cdot G(C_S^Mn) \quad [3]$$

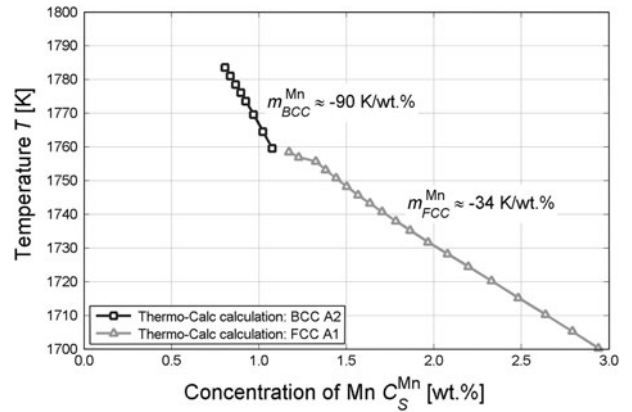


Fig. 8—Concentration of Mn in the solid with decreasing temperature; calculation performed with Thermo-Calc Classic.

The curvature influence on the concentration pattern can be considered optionally at this stage of the reconstruction process.^[39] However, the calculations based on the measured and smoothed concentration maps showed that the curvature hardly affects the shape of the reconstructed dendrites and that its influence can be neglected for the investigated steel.

E. Creating the Dendritic Structure

Finally, the reconstruction of the dendritic structure was achieved by connecting all array entries C_S^Mn with the same predefined threshold concentration of Mn. The connection surfaces represent the shape of the dendrites at a certain stage of solidification. In Figure 9, the obtained structures for 1.05 wt pct Mn are depicted without (Figure 9(a)) and with (Figure 9(b)) consideration of the temperature gradient on the concentration field. It is obvious that the effect of the occurring temperature gradient on the investigated microsegregation pattern and, therefore, on the dendrite's shape is crucial. Whereas the dendrites in Figure 9(a) have almost the same thickness from the top to the bottom of the reconstruction domain, their thickness decreases in Figure 9(b) along the growth direction as expected for columnar solidification.

III. RESULTS AND DISCUSSION

A. Visualizing the Dendritic Growth

Varying the predefined threshold concentration enables visualizing the dendritic growth. For example, three dendritic structures at different solidification stages are depicted in Figure 10 depending on ascending isoconcentrations. Exporting the surface coordinates of these structures makes them available for subsequent processing in numerical simulation tools.

B. Structure Evaluation

To describe the evolution of the dendritic surface area A_{SL} , which represents the solid-liquid interface between

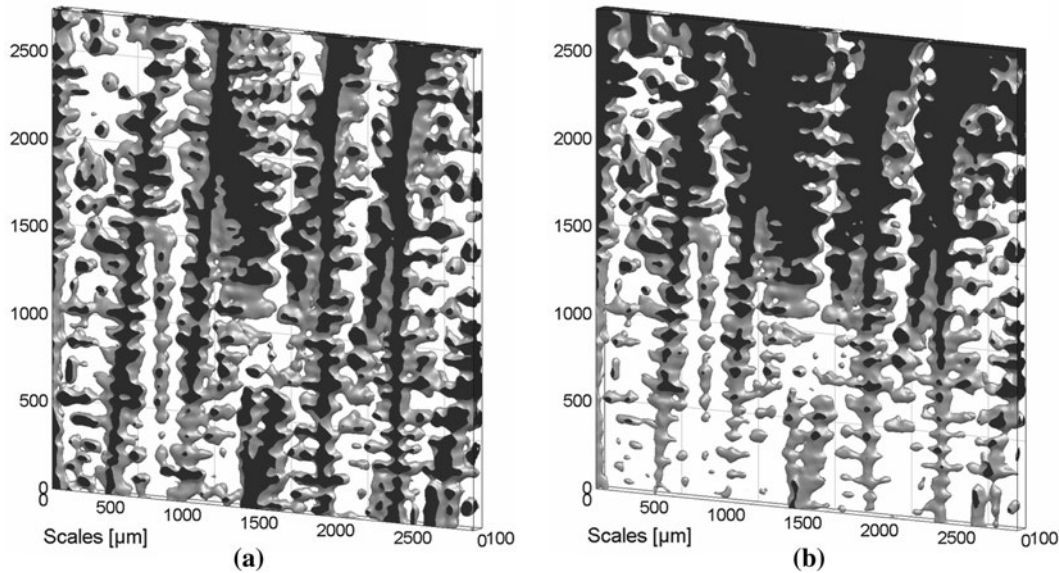


Fig. 9—Dendritic structures without (a) and with (b) considering the temperature gradient on the concentration pattern. The concentrations of Mn at the dendritic surface, $C_{S''}$ (a) and $C_{S''}$ (b), is 1.05 wt pct in both cases.

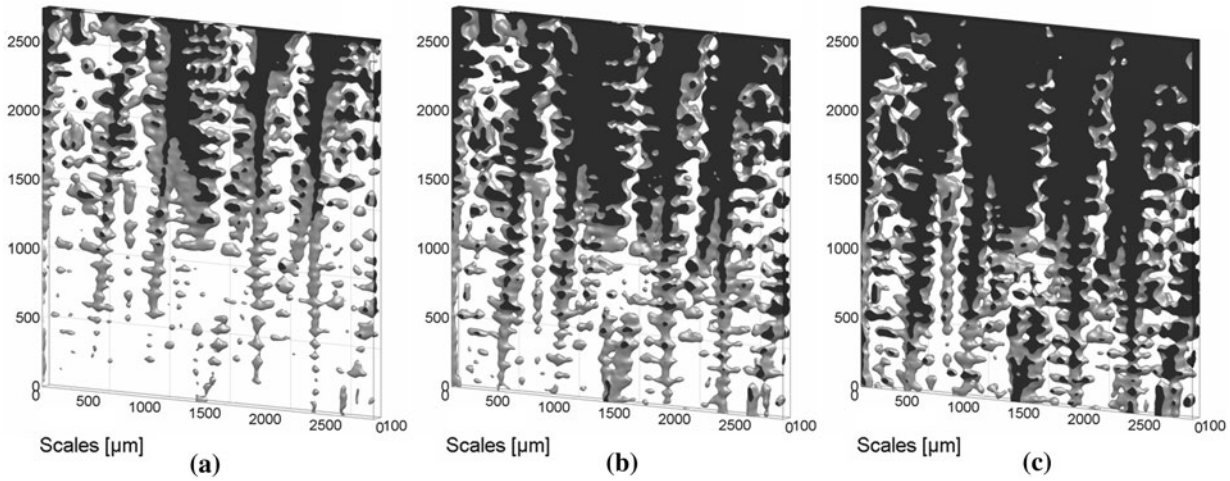


Fig. 10—Dendritic structure depending on three different surface concentrations of Mn: (a) $C_{S''} = 1.00$ wt pct Mn, (b) $C_{S''} = 1.05$ wt pct Mn, and (c) $C_{S''} = 1.10$ wt pct Mn. Each concentration correlates with the shape of the dendritic structure at a certain moment of solidification.

the melt and the forming dendrites, the area-volume ratios $S_{V,T}$ and $S_{V,S}$ are introduced. Because the presented reconstruction method is based on solid phase concentrations solely, “liquid” means the sample domain containing higher concentration values and “solid” is the domain containing lower concentration values than the predefined value for visualizing the dendritic surface. $S_{V,T}$ and $S_{V,S}$ are defined as shown in Eqs. [4] and [5], where the dendritic surface area A_{SL} is related to the total volume of the reconstruction domain V_T or to the volume of the developing solid V_S , respectively.

$$S_{V,T} = \frac{A_{SL}}{V_T} \quad [4]$$

$$S_{V,S} = \frac{A_{SL}}{V_S} \quad [5]$$

Depending on the solid fraction f_S , the curves for these ratios are illustrated in Figure 11 afterward. Notice that f_S represents the average solid fraction of the entire dendritic structure. It is apparent that $S_{V,T}$ has a maximum value at $f_S \approx 0.5$, whereas it becomes zero at $f_S = 0.0$ and $f_S = 1.0$. However, with increasing solid fraction, $S_{V,S}$ decreases rapidly toward zero. One can approximate the depicted curve for $S_{V,T}$ with the generally known relationship

$$S_{V,T} = c \cdot f_S^a \cdot (1 - f_S)^b \quad [6]$$

where the empirical constant c as well as the exponents a and b are chosen to fit the experimental data. Several proposals can be found for a and b in the literature, such as $a = b = 1$ (Speich and Fisher^[40]), $a = b = 2/3$ (Cahn^[41]), or $a = 0.517$, $b = 0.467$ (Limodin *et al.*^[20] according to Rath^[42]). Furthermore, Ratke and

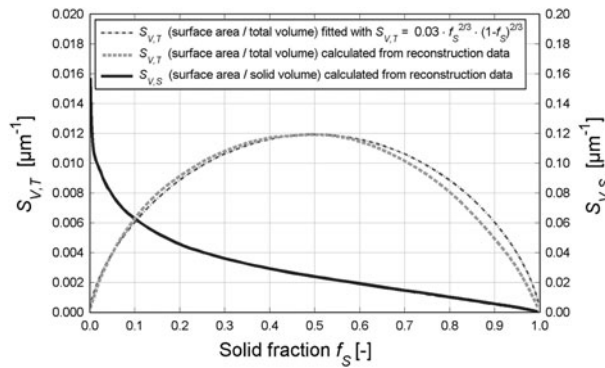


Fig. 11—Solid–liquid interface area ratios depending on the solid fraction. The depicted curves were calculated from the structure that was obtained after considering the temperature gradient.

Genau^[43] derived an analytical model to describe the evolution of the specific surface area during solidification using $a = 1/2$ and $0 < b < 1$. For the obtained dendritic structure, it is possible to approximate $S_{V,T}$ using Eq. [6] with $c = 0.03 \mu\text{m}^{-1}$ and $a = b = 2/3$. Figure 11 shows that this approximation fits well for $f_s < 0.5$, whereas it deviates slightly for $f_s > 0.5$.

C. Final Remarks

For the reconstruction method presented in this article, the following concluding remarks should be taken into consideration:

1. To cover the entire solidification range of a dendritic structure, only a single sample has to be investigated by microprobe analysis. This is beneficial for simulations that require a certain 3-D structure at a series of different solid fractions (*e.g.*, for permeability calculations based on CFD simulations).
2. The presented structure consists of five concentration maps taken from different depths of the sample. Accounting to the chosen distance between each of these maps, the final structure has a thickness of $100 \mu\text{m}$, which is a small extension compared with its length and width. Thus, to obtain a representative shape of the dendrites in depth direction, it would be necessary to increase the number of maps.
3. Because the investigated steel sample was taken from an industrially produced continuous casting slab, it contains several alloying elements. All of these elements affect more or less the solidification behavior of the steel, which cannot be covered analytically. For fundamental investigations on the solidification structure, it would be interesting to focus on a binary alloy cast under well-known thermal conditions (*e.g.*, inside a Bridgman furnace).
4. The application of the presented method is limited to metals that contain alloying elements with a high microsegregation tendency on the one hand and a small diffusivity inside the solid on the other hand. For steels, Mn fulfills both of these conditions, whereas carbon fails to meet them because of its

strong solid-state diffusivity.

5. Measurement uncertainties, the estimation of unknown quantities (*e.g.*, of the temperature gradient G), and unconsidered coarsening and diffusion mechanisms indicate the presented structure to show a more likely approximation of the steel dendrites instead of an exact representation based on a fundamental understanding of the basic solidification behavior in directionally cast metals.

ACKNOWLEDGMENTS

The authors thank the industrial project partners Materials Center Leoben Forschung GmbH (MCL), voestalpine Stahl GmbH, voestalpine Stahl Donawitz GmbH & Co KG, and Siemens VAI Metals Technologies GmbH & Co for their contributions to this project. Thanks are due to Mrs. Judith Fluch from voestalpine Stahl GmbH as well as to Mrs. Federica Zaccarini and Mr. Helmut Mühlhans from the University of Leoben for supporting the microprobe measurements. Special thanks are due to Mr. Siegfried Schider from the Materials Center Leoben Forschung GmbH for the excellent sample preparation.

NOMENCLATURE

C_S	concentration measured with the microprobe (wt pct)
$C_{S'}$	concentration after applying the median filter (wt pct)
$C_{S''}$	concentration after applying the Gaussian filter (wt pct)
$C_{S'''}$	concentration after the temperature gradient correction (wt pct)
σ	standard deviation of the Gaussian filter (px)
$R_{x,y}$	filter area that surrounds a certain map pixel
i, j	Cartesian coordinates of the filter area in two dimensions (px)
x, y	Cartesian coordinates of the microprobe map in two dimensions (px)
X, Y	Cartesian coordinates of the continuous casting strand in two dimensions (mm)
T	temperature (K)
G	temperature gradient (K/mm)
f_s	solid fraction (-)
ΔC_G	concentration difference from the temperature gradient (wt pct)
C_S^{Mn}	concentration of Mn in the solid (wt pct)
m^{Mn}	ratio between the temperature and the Mn concentration in the solid (K/wt pct)
$m_{\text{bcc}}^{\text{Mn}}$	ratio for the body-centered cubic phase (K/wt pct)
$m_{\text{fcc}}^{\text{Mn}}$	ratio for the face-centered cubic phase (K/wt pct)
A_{SL}	surface area of the dendrites (solid–liquid interface area) (μm^2)
V_S	volume of the solid dendrites (μm^3)

V_T	volume of the entire reconstruction domain (μm^3)
$S_{V,S}$	ratio between the surface area and the solid volume (μm^{-1})
$S_{V,T}$	ratio between the surface area and the entire volume (μm^{-1})
a, b	fitting parameters (-)
c	fitting parameter (μm^{-1})
λ_1	primary dendrite arm spacing (μm)
λ_2	secondary dendrite arm spacing (μm)

REFERENCES

1. R.T. DeHoff: *J. Microsc.*, 1983, vol. 131, pp. 259–63.
2. J. Madison, J. Spowart, D. Rowenhorst, L.K. Aagesen, K. Thornton, and T.M. Pollock: *Acta Mater.*, 2010, vol. 58, pp. 2864–75.
3. D. Bernard, Ø. Nielsen, L. Salvo, and P. Cloetens: *Mater. Sci. Eng. A*, 2005, vol. 392, pp. 112–20.
4. D. Fuloria, P.D. Lee, and D. Bernard: *Mater. Sci. Eng. A*, 2008, vol. 494, pp. 3–9.
5. E. Khajeh and D.M. Maijer: *Acta Mater.*, 2010, vol. 58, pp. 6334–44.
6. J. Domitner, C. Hözl, A. Kharicha, M. Wu, A. Ludwig, M. Köhler, and L. Ratke: *IOP C. Ser. Mater. Sci. Eng.*, 2011, vol. 27, 012016, pp. 1–6.
7. M.V. Kral, M.A. Mangan, G. Spanos, and R.O. Rosenberg: *Mater. Charact.*, 2000, vol. 45, pp. 17–23.
8. M. Li, S. Ghosh, T.N. Rouns, H. Weiland, O. Richmond, and W. Hunt: *Mater. Charact.*, 1998, vol. 41, pp. 81–95.
9. N. Chawla, V.V. Ganesh, and B. Wunsch: *Scripta Mater.*, 2004, vol. 51, pp. 161–65.
10. N. Chawla, R.S. Sidhu, and V.V. Ganesh: *Acta Mater.*, 2006, vol. 54, pp. 1541–48.
11. J. Alkemper and P.W. Voorhees: *J. Microsc.*, 2001, vol. 201, pp. 388–94.
12. J.E. Spowart, H.M. Mullens, and B.T. Puchala: *JOM*, 2003, vol. 55, pp. 35–37.
13. J.E. Spowart: *Scripta Mater.*, 2006, vol. 55, pp. 5–10.
14. J. Alkemper and P.W. Voorhees: *Acta Mater.*, 2001, vol. 49, pp. 897–902.
15. D. Kammer and P.W. Voorhees: *Acta Mater.*, 2006, vol. 54, pp. 1549–58.
16. J.L. Five and P.W. Voorhees: *Acta Mater.*, 2009, vol. 57, pp. 2418–28.
17. J. Madison, J.E. Spowart, D.J. Rowenhorst, and T.M. Pollock: *JOM*, 2008, vol. 60, pp. 26–30.
18. M. Schaffer, J. Wagner, B. Schaffer, M. Schmied, and H. Mulders: *Ultramicroscopy*, 2007, vol. 107, pp. 587–97.
19. O. Ludwig, M. DiMichiel, L. Salvo, M. Suéry, and P. Falus: *Metall. Mater. Trans. A*, 2005, vol. 36A, pp. 1515–23.
20. N. Limodin, L. Salvo, E. Boller, M. Suéry, M. Felberbaum, S. Gailliègue, and K. Madi: *Acta Mater.*, 2009, vol. 57, pp. 2300–10.
21. J.A. Spittle and S.G.R. Brown: *J. Mater. Sci.*, 1995, vol. 30, pp. 3989–94.
22. D.J. Jarvis, S.G.R. Brown, and J.A. Spittle: *Mater. Sci. Technol.*, 2000, vol. 16, pp. 1420–24.
23. S.G.R. Brown, J.A. Spittle, D.J. Jarvis, and R. Walden-Bevan: *Acta Mater.*, 2002, vol. 50, pp. 1559–69.
24. M. Rappaz and Ch.-A. Gandin: *Acta Metall. Mater.*, 1993, vol. 41, pp. 345–60.
25. Ch.-A. Gandin and M. Rappaz: *Acta Metall. Mater.*, 1994, vol. 42, pp. 2233–46.
26. Ch.-A. Gandin and M. Rappaz: *Acta Mater.*, 1997, vol. 45, pp. 2187–95.
27. A. Karma and W.-J. Rappel: *Phys. Rev. Lett.*, 1996, vol. 77, pp. 4050–53.
28. A. Karma and W.-J. Rappel: *Phys. Rev. E*, 1998, vol. 57, pp. 4323–49.
29. J.-H. Jeong, N. Goldenfeld, and J.A. Dantzig: *Phys. Rev. E*, 2001, vol. 64, p. 041602.
30. B. Nestler, A. Aksi, and M. Selzer: *Math. Comput. Simulat.*, 2010, vol. 80, pp. 1458–68.
31. S. Ilie, H. Preßlinger, P. Reisinger, M. Mayr, and K. Etzelsdorfer: *Steel Res. Int.*, 2007, vol. 78, pp. 327–32.
32. M. Mayr: Voestalpine Stahl GmbH, Linz, unpublished research, 2003.
33. R.C. Gonzalez, R.E. Woods, and S.L. Eddins: *Digital Image Processing Using MATLAB*, 3rd ed., Prentice Hall, Upper Saddle River, NJ, 2004, pp. 159–60.
34. W. Burger and M.J. Burge: *Digitale Bildverarbeitung*, 2nd ed., Springer-Verlag, Berlin, Germany, 2006, pp. 89–100.
35. A. Ludwig, M. Gruber-Pretzler, M. Wu, A. Kuhn, and J. Riedle: *FDMP*, 2005, vol. 1, pp. 285–300.
36. A. Ludwig and M. Wu: *Mater. Sci. Eng. A*, 2005, vols. 413–414, pp. 109–14.
37. M. Wu and A. Ludwig: *Metall. Mater. Trans. A*, 2006, vol. 37A, pp. 1613–31.
38. Foundation of Computational Thermodynamics: Thermo-Calc® Database Guide. Thermo-Calc Software AB, Stockholm, 2006.
39. J. Domitner, A. Kharicha, M. Grasser, and A. Ludwig: *Steel Res. Int.*, 2010, vol. 81, pp. 644–51.
40. G.R. Speich and R.M. Fisher: *Recrystallization, Grain Growth and Textures*, ASM, Materials Park, OH, 1966, pp. 563–98.
41. J.W. Cahn: *Trans. TMS-AIME*, 1967, vol. 239, pp. 610–16.
42. B.B. Rath: *Solid-Solid Phase Transformations*, TMS-AIME, Warrendale, PA, 1982, pp. 1097–103.
43. L. Ratke and A. Genau: *Acta Mater.*, 2010, vol. 58, pp. 4207–11.